SHAPE AND POSE RECOVERY OF SOLAR-ILLUMINATED SURFACES FROM COMPRESSIVE SPECTRAL-POLARIMETRIC IMAGE DATA

Sudhakar Prasad
Department of Physics and Astronomy, University of New Mexico, Albuquerque, NM 87131

Qiang Zhang
Dept. of Biostatistical Sciences, Wake Forest University, Winston-Salem, NC 27109

Robert Plemmons
Dept. of Mathematics and Computer Science, Wake Forest University, Winston-Salem, NC 27109

We present simulation-based studies of the use of compressively sensed spectral-polarimetric spatial image data from a solar-illuminated reflecting surface to recover its material signature, three-dimensional (3D) shape, pose, and degree of surface roughness. The spatial variations of the polarimetric BRDF around glint points contain unique information about the shape and roughness of the reflecting surface that is revealed most dramatically in polarization-difference maps from which the spatially generalized diffuse-scattering contibutions to brightness are largely absent. Here we employ a specific compressed-sensing protocol, the so-called Coded-Aperture Snapshot Spectral Polarimetric Imager advanced recently by Tsai and Brady, to simulate noisy measurements from which these surface attributes are recovered in a sequential manner. Even in the presence of additive sensor noise, the recovery of these surface attributes for roughened, highly reflecting surfaces seems to be quite robust.

1 Introduction

Hyperspectral image datasets typically contain far more information than needed for a typical remote sensing task of material identification, segmentation, and composition. For example, a typical solar-illuminated man-made satellite consists of a relatively small number of geometrical primitives and materials with unique spectral and polarimetric reflectance signatures. This implies a highly correlated hyperspectral image (HSI) datacube, which may be idealized as a low-rank sum of terms, each expressible in a spatial-spectral factorized form. Because of this underlying high sparsity, compressed sensing protocols such as the Coded-Aperture Snapshot Spectral Polarimetric Imager (CASSPI) [1] tend to provide for excellent recovery of the HSI datacube in each non-vanishing polarimetric Stokes component.

The sparsity of the spectral-polarimetric (SP) brightness distribution reflected by such an object may be expressed uniquely in terms of a relatively small set of parameters that characterize its reflecting surfaces, notably their shape and size, relative orientation, metallicity, roughness, and material composition. The robustness of the recovery of such parameters from compressive SP image data is an inverse problem that requires a comprehensive physical model for mapping these parameters to the electromagnetic data space. Our algorithm for this inverse problem is non-iterative but sequential in which the material composition of a single elementary surface is first extracted from the uniform brightness of its diffusely reflecting regions whose shape, size, and roughness parameters do not affect its spectral signature, followed by a recovery of its shape and pose parameters. The full forward model is composed of the physical model that yields the polarimetric bi-directional reflectance distribution function (pBRDF) [2] and the CASSPI observation model that maps the pBRDFs so obtained into the final compressive 2D observations of the CASSPI instrument.

In this paper we present a physical model describing the pBRDF for a highly reflecting surface of nontrivial 3D shape, whose roughness may be described accurately via the microfacet roughness model. For definiteness, the 3D object is taken to belong to the superquadric family of shapes, that is characterized fully in terms of a small number of parameters. The spatial-spectral pBRDFs obtained for this object under solar illumination are then fed into the CASSPI data model, which generates a noisy simulation of spatially-spectrally compressed, coded two-dimensional data. Because of the high sparsity of the object representation, the problem of extracting the shape and roughness parameters as well as the orientation of the object relative to some fixed axes is a highly over-determined inverse problem, as we demonstrate in this paper. For highly reflecting objects like the one considered here, the spectral content of the reflected light is essentially the same as that of the solar radiation that illuminates it, making the spectral recovery a trivial problem.

2 Physical Model for the Polarimetric BRDF

Our physical model follows closely the work of Hyde, *et al.* [2], in which the polarimetric signature of the surface is carried entirely by the single-scattering, or specular, component of the solar reflectance function. The power spectrum of the specular component is largely independent of the material composition of the surface, being propotional to the solar power spectrum over the observational bands. By contrast, the material composition of the surface, together with its roughness, strongly influence the power spectrum of the multiple-scattering, or diffuse, component of reflectance from a roughened surface. The latter is essentially Lambertian but still dependent on the 3D geometry of the surface that affects its illumination locally, and when added to the former yields the total BRDF.

Locally the polarimetric BRDF depends on the directions of solar illumination and observation relative to the local mean-surface normal and on the surface roughness. For fixed illumination and observation directions, the bisector of the angle formed by them defines the direction of the true surface normal for all surface elements that can contribute to the observed specular reflection. For surfaces that are perfectly smooth, this means only isolated "glint" points which specularly reflect into the observation direction, but for rough surfaces there exists a finite probability that all points in a neighborhood surrounding such a glint point have a local surface orientation meeting this specularity condition. Assuming an azimuthally invariant probability distribution function (PDF) $P(\alpha;\sigma_\alpha)$ of the fluctuating surface normal with respect to the mean surface normal, where α is the angle between these two directions and σ_α its standard deviation, then it is clear that the BRDF must be proportional to $P(\alpha;\sigma_\alpha)$, provided the fluctuating surface normal is taken to be parallel to the solar-angle bisector. The surface height fluctuations about the mean surface also yield either an obstructed illumination ("shadowing") or obstructed observation ("masking") near grazing angles at which neighboring elements of the rough surface can shield one another [3]. If Q denotes this shadowing-masking function, which depends on the angles of incidence and reflection relative to the mean surface and fluctuating surface elements, then the specular BRDF must be proportional to Q as well. When combined with other geometrical area-projection cosine factors and the Fresnel reflection coefficients $|r_s|^2$ and $|r_p|^2$ for the s and p polarizations defined relative to the solar illumination plane, these considerations yield the following specular BRDF for the first two components of the polarimetric Stokes vector observed in reflection from the point (x,y) of the surface at wavelength λ:

$$\begin{aligned} F_0(x,y,\lambda) &= \frac{P(\alpha;\sigma_\alpha)\,Q}{4\cos\theta_i\cos\theta_r\cos\alpha} S_\odot(\lambda)\frac{1}{2}(|r_s(\lambda)|^2+|r_p(\lambda)|^2); \\ F_1(x,y,\lambda) &= \frac{P(\alpha;\sigma_\alpha)\,Q}{4\cos\theta_i\cos\theta_r\cos\alpha} S_\odot(\lambda)\frac{1}{2}(|r_s(\lambda)|^2-|r_p(\lambda)|^2), \end{aligned} \tag{1}$$

where α denotes the angle between the unit mean-surface normal $\hat{n}(x,y)$ and the unit solar-angle bisector vector, $\hat{n}_\odot$, and is given by

$$\cos\alpha = \hat{n}(x,y)\cdot\hat{n}_\odot \tag{2}$$

and the angles of incidence and reflection relative to the mean surface are given by the equations

$$\cos\theta_i = \hat{n}_i\cdot\hat{n}(x,y),\ \ \cos\theta_r = \hat{n}_r\cdot\hat{n}(x,y). \tag{3}$$

The symbol $S_\odot(\lambda)$ denotes the spectral profile of the sun as a function of the wavelength λ. The s and p polarization components of the specular pBRDF, which we denote as F_s and F_p, are simply the sum and difference, $F_s = F_0 + F_1$ and $F_p = F_0 - F_1$.

The shadowing-masking factor Q occurring in the preceding expressions depends on the specific roughness model consistent with the history of damage of a specific metallic or dielectric surface. For the so-called microfacet model in which the surface can be regarded as fluctuating about the mean surface via locally flat microfacets, this factor has been well studied, and approximate forms of it have been given [4]. The present paper uses this roughness model. Our continuing work, however, is focused on first generalizing the microfacet model to the hemispherical pit model [5] in which a surface has been roughened by bombardment by sand particles or other microdebris. Indeed, a still more general roughness model is a composite model in which a number of different roughening mechanisms may be simultaneously operative, and a statistical mixture of the various elementary models must be created with appropriate relative weights that reflect the relative frequency of different roughness primitives (facets, pits, etc). Each polarimetric component of the overall BRDF in this composite model is given simply by a weighted sum over the same components of the BRDFs for the different elementary models [6].

The spectral shape of the BRDF is determined by the product of $S_\odot$ and the dependence of the Fresnel reflection coefficients $|r_s|^2$ and $|r_p|^2$ on the wavelength due to the dispersion of the material's index of refraction. The vectors,

$\hat{n}_i$ and $\hat{n}_r$, are the unit vectors from the surface element to the sun and the observer, respectively. Since the solar illumination is unpolarized, the other two components of the Stokes vector, as one may easily show, vanish identically. Note that the BRDFs depend on the roughness of the surface through the standard deviation σ_α of the surface orientations relative to the mean surface.

The diffuse component of the reflected radiance may be computed by subtracting out the specular BRDFs (1) from the overall BRDFs in which the masking factor, but not the shadowing factor that controls overall illumination, is absent. Including the masking factor ensures the inclusion of only the single-scattering contribution, and dropping it thus permits us to include multiple scattering contributions as well. While the latter are the most significant contributions to diffuse scattering, a part is also contributed by the reradiation of the refracted light that penetrates the surface and is absorbed by the material under the surface. We can neglect this indirect contribution, however, as it occurs at wavelengths that are much longer than the optical-NIR wavelengths of interest. Since the diffuse scattering is largely unpolarized and emitted nearly isotropically in the forward half-space, *i.e.,* it is Lambertian, it only contributes to the first Stokes component of the BRDF the amount

$$\begin{aligned} F_0^{(diffuse)} =& \frac{\int_+ [F_{0,shadow} - F_0] \cos\theta_r d^2\Omega_r}{\int_+ \cos\theta_r \, d^2\Omega_r} \\ =& \frac{1}{\pi} [F_{0,shadow} - F_0] \cos\theta_r \, d^2\Omega_r, \end{aligned} \tag{4}$$

where the symbol $F_{0,shadow}$ refers to the expression (1) for F_0 in which the shadowing/masking function Q has been replaced by a pure shadowing function Q_1. The subscript $+$ on the integrals in expression (4) indicates solid-angle integration over the forward half-space, $0 \leq \theta_r \leq \pi/2$, $0 \leq \phi_r < 2\pi$. It is worth noting that the diffuse scattering, while isotropically distributed, does depend on the angle of incidence of the sunlight on the surface and thus for a curved surface of general 3D shape varies, in general, across such a surface. Like the specular single-scattering contribution, it too thus carries information about the 3D shape of the surface. We also note that our expression (4) for the diffuse BRDF is more general than the expression suggested in Ref. [2].

In Fig. 1 we present surface plots of the specular and diffuse BRDFs for a 3D superquadric shape built out of aluminum for which the complex refractive index has been tabulated [7] over the wavelength range 0.4 - 2.4 μm of interest to the present work. The difference polarimetric map of the specular BRDF is also shown in this figure. All figures refer to the specific wavelength of 0.4 μm and a fixed solar phase angle $2\beta = 2\pi/5$. The equation of a superquadric, a generalization of so-called quadric surfaces such as ellipsoids and hyperboloids, is given via the following parameterization [8, 9]:

$$\left[\left(\frac{|x|}{a} \right)^{2/\epsilon_2} + \left(\frac{|y|}{b} \right)^{2/\epsilon_2} \right]^{\epsilon_2/\epsilon_1} \pm \left(\frac{|z|}{c} \right)^{2/\epsilon_1} = 1, \tag{5}$$

where the parameter set include the three scale parameters, a, b, c, and two shape parameters, ϵ_1, ϵ_2, which are all positive. In our work, we chose the positive sign for the last term on the left side of this equation, for which the solid is singly connected and topologically equivalent to an ellipsoid. The orientation of the superquadric relative to the line of sight from the observer can also be specified in terms of three Euler angles, α, β, γ. The following values were chosen for these eight parameters for the superquadric surface used in the present work: $a = b = c = 2$; $\epsilon_1 = \epsilon_2 = 1.5$; and $\alpha = 1 \; rad$, $\beta = \gamma = 0$.

We easily see from these color-coded plots that both the polarization-difference and polarization-sum maps of the specular BRDF are rather localized with much larger fractional intensity variations over much shorter length scales than the unpolarized, diffuse component of the total BRDF. The latter, as we had noted earlier, is spatially more generalized. This localization disparity between the specular and diffuse components holds only if the surface has a reasonably high degree of roughness, represented by the reciprocal of the ratio of the mean microfacet length to the standard deviation of microfacet heights about its zero mean value, namely l/σ_h. The results shown here refer to the moderate-roughness scenario, $l/\sigma_h = 2$. We also note that, although not shown, the spectral shape of any of the three BRDFs exhibited here is pretty much the same as that of the solar spectrum since in Eqs. (1) and (4) all of the reflection coefficients, $|r_s|^2$ and $|r_p|^2$, at all of the wavelengths in the range are essentially close to 1, with little variation from one wavelength to the next. This is so because aluminum is highly reflecting at all of these wavelengths, and thus is essentially white under solar illumination.

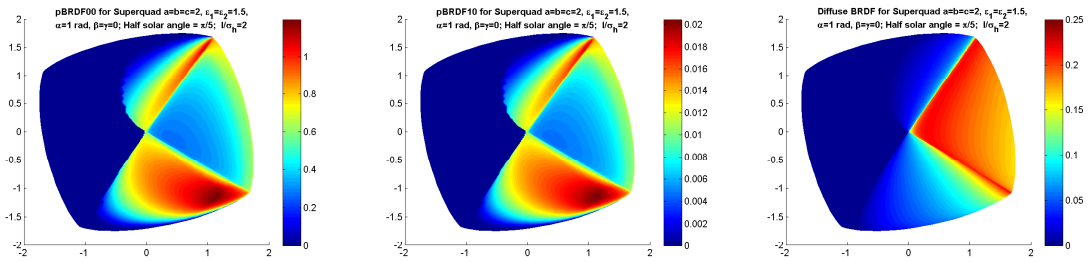

(a) (b) (c)

Figure 1: (a) The total (polarization-sum) specular BRDF; (b) the polarization-difference specular BRDF; and (c) the unpolarized diffuse BRDF which has a Lambertian radiance profile; all evaluated at the wavelength 0.4 μm for the chosen superquadric which is illuminated by the sun at the solar half angle $\beta = \pi/5$.

3 The CASSPI Model

In the polarimetric CASSI instrument, the s and p linear polarizations, defined relative to the sun-object-observer plane, are separated onto different regions of the broadband sensor array by means of two plane-parallel birefringent crystals with optic axes that are mutually orthogonal. In this sense, the polarimetric signal components are not compressed, while the dispersion inherent in the birefringent crystals yields image-plane-coded spectral-spatial compression of the observed data. The forward model for CASSPI thus is merely a doubled-up version of the usual SD-CASSI model. A new design of the CASSPI instrument with a liquid-crystal spatial light modulator (LC-SLM) and a polarizer replacing the birefringent crystals [10] will achieve a more comprehensive compression across spectral, polarimetric, and spatial domains, and will permit an extraction of all four components of the polarimetric Stokes vector.

The s and p polarization components of the BRDF are transformed into the following CASSPI data distributions:

$$G(x,y) = \sum_{i=s,p} \int F_i(x - \alpha\,\delta\lambda - x_i, y, \lambda)\, t(x - \alpha\,\delta\lambda - x_i, y)\, w(\lambda)\, d\lambda \; + \epsilon(x,y), \tag{6}$$

where $w(\delta\lambda)$ is the spectral sensitivity function for the wideband CASSPI sensor, x_i, $i = s, p$, are the displacements of the two polarizations at a reference wavelength λ_R caused by the birefringent crystals, and α is the coefficient of dispersion of the crystals, assumed identical for the two, which determines how far the signal at a particular wavelength is spatially displaced relative to the signal at the reference wavelength λ_R. The symbol $\delta\lambda$ denotes the difference $(\lambda - \lambda_R)$. The image-plane code $t(x, y)$ is an amplitude transmission code whose linear pixel size is roughly 4-7 times the sensor pixel size. We have also explicitly indicated the spatial and spectral variations of each polarimetric BRDF component by appending the wavelength λ in the list of its arguments. $\epsilon_s(x, y)$ represents the white noise, $N(0, \sigma^2)$. Note that in sum (6) F_s and F_p each consist of both the specular component, given by the sum and difference of the two equations in (1), respectively, and the diffuse component, given by half of expression (4) per polarization.

A simulated noisy CASSPI image of the superquadric object in Fig. 1 is shown in Fig. 2, with $\sigma = 0.05$ or SNR$= \mu/\sigma = 6.37$, where μ is the mean of all nonzero elements in F_i. Comparing with the BRDF functions, $F_i(x, y, \lambda), i = s, p$, at the 400nm wavelength, we can see the dispersions in both x and y directions due to the displacements by the birefringent crystals, in the support of the noiseless CASSPI image at the very right. It is hard to see this in the simulated CASSPI image because of the small scales of dispersed radiance, especially in the vertical direction since F_1 is often much smaller than F_0, because $r_s^2 + r_p^2 \gg r_s^2 - r_p^2$ in Eqs. (1).

3.1 Results

To recover the full BRDF functions, $F_i(x, y, \lambda)$ from the compressed measurements, $g(x, y)$, we need to solve a highly under-determined linear system. Notice, however, that $F_i(x, y, \lambda)$, in its discrete form, can be unfolded into a matrix, $F_i \in \mathbb{R}^{mn \times d}$, where m and n are the pixel numbers in x and y directions, and d is the number of spectral channels. Note that because of its form (1) this matrix is rank-one. The singular values of the simulated F_i in Fig. 1, where the two largest singular values are $s_1 = 288.3$, and $s_2 = 0.659$, also illustrate this fact.

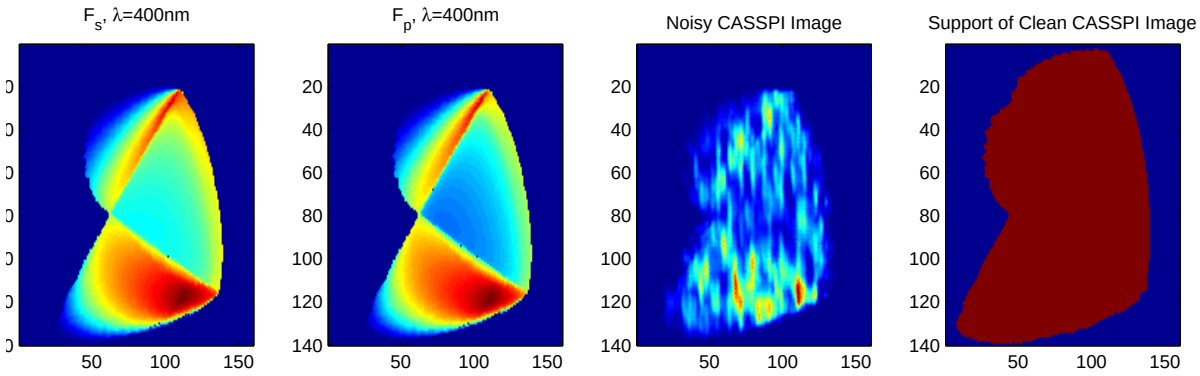

Figure 2: A simulated CASSPI image using the object illustrated in Fig. 1.

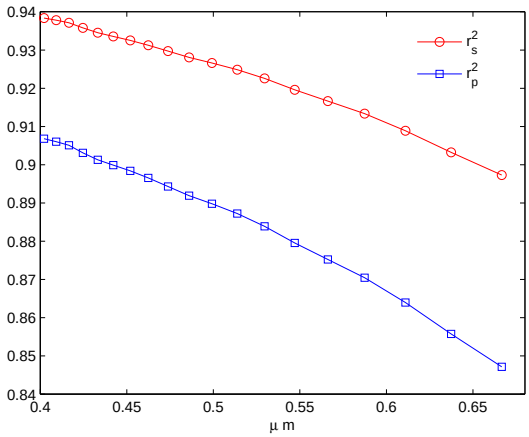

Figure 3: The approximate wavelength-independency of r_s and r_p to the first order.

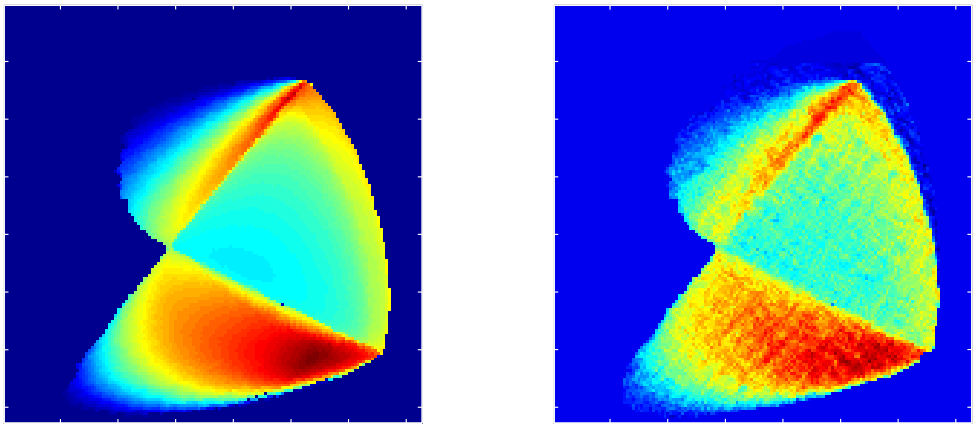

Figure 4: Comparison of the reconstructed wavelength-independent part of the pBRDF function with the true one.

The approximate wavelength independence of the Fresnel reflection coefficients, r_s and r_p, which we can easily appreciate from the plot in Fig. 3, further simplifies the inverse problem by turning it into an exact problem, i.e., the number of knowns is the same as the number of unknowns. In the presence of noise, we can use Tikhonov regularization to seek smooth least-square solutions as the following:

$$\min_f \|g - Af\|_2^2 + \beta\|f\|_2^2, \tag{7}$$

where g is the vectorized discrete $G(x, y)$, A is the system matrix depending on discretized $t(x, y)$, $w(\lambda)$ and $S_\odot(\lambda)$ in Eq. (6), f is the vectorized F by concatenating vectorized F_s and F_p, and β is the regularization parameter depending on the noise level. Figure 4 shows the reconstructed wavelength-independent part of the BRDF functions in Eqs. (1), compared with the true one, i.e.,

$$\tilde{F}(x, y) = \frac{P(\alpha; \sigma_\alpha)\, Q}{4\cos\theta_i \cos\theta_r \cos\alpha} + \frac{1}{\pi}\int \frac{P(\alpha; \sigma_\alpha)\,(Q_1 - Q)}{4\cos\theta_i \cos\theta_r \cos\alpha} \cos\theta_r d^2\Omega_r, \tag{8}$$

where

$$Q = \min\left[1, \frac{2\cos(\alpha)\cos(\theta_r)}{\cos(\beta)}, \frac{2\cos(\alpha)\cos(\theta_i)}{\cos(\beta)}\right], \quad Q_1 = \min\left[1, \frac{2\cos(\alpha)\cos(\theta_i)}{\cos(\beta)}\right]$$

are the shadowing-masking and shadowing-only factors we talked about earlier.

From the reconstructed $\tilde{F}(x, y)$, we can further estimate the shape, pose and surface roughness parameters. Because the problem is highly nonlinear, it is hard to derive the gradients of a least-squares functional against parameters, we choose to use an adaptive random-walk optimization algorithm, namely the Cuckoo search algorithm [11]. Given the range of the parameters' search space, the algorithm searches for the optimal point estimate in a descending order, within a preset iteration limit. It is especially suitable for complicated objective functions, such as the specular and diffuse BRDF functions. Table 1 lists the estimated parameters compared with the true ones, and we observe reasonably good estimates, except in the three Euler angles. However, due to the symmetry of the superquadric object, this combination of Euler angles brings out the same pose as the true values, as shown in Fig. 5, a very close resemblance between the reconstructed wavelength-independent part of the pBRDF functions, $\tilde{F}(x, y)$, and the true one.

4 Conclusions

In this paper we have studied in simulation the use of compressive spectral-spatial reflectance data from highly reflecting, metallic surfaces to recover their shape and orientation parameters for a low-dimensional family of simple

Table 1: The estimated parameters are compared with the true ones.

	a	b	c	ϵ_1	ϵ_2	α	β	γ	σ_l
True	2.00	2.00	2.00	1.5	1.5	1.00	0.00	0.00	2.00
Estimated	1.931	1.974	1.939	1.423	1.251	0.059	0.5730	1.571	1.987

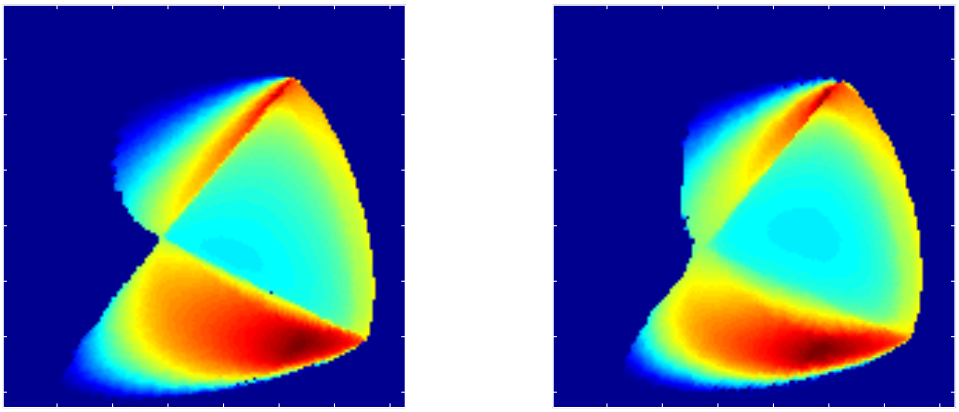

Figure 5: Comparison of the reconstructed wavelength-independent part of the BRDF functions with the true one, using the estimated shape and surface parameters.

shapes. The forward model used in the solution of the inverse problem via nonlinear optimization employs a generalization of the polarimetric BRDF formulas derived previously for the micro-facet-based roughness model. The polarimetric information, as contained in the polarization-difference BRDF map which includes only singly-reflected light, is more localized around the glint points of the surface, while the polarization-sum BRDF map containing the diffuse, multiply-reflected light is spatially more generalized. For more general shapes than the one considered here, the former may provide more robust information about how the shape changes in the vicinity of glint spots. We are currently in the process of extending our present work to include more general object shapes, for which the spatial variations of the BRDF can provide information about the local curvatures of the surface, which can be used in turn to infer its 3D shape. Our treatment will be further generalized to include both instrumental and turbulence-induced image blurs.

Acknowledgment

The work reported here was supported by the US Air Force Office of Scientific Research under award numbers FA9550-08-1-0151, FA9550-09-1-0495 and FA9550-11-1-0194.

References

[1] T.-H. Tsai and D. Brady, "Coded-aperture snapshot spectral polarimetric imager," Appl. Opt., vol. 52, pp. 2153-2161 (2013).

[2] M. Hyde, J. Schmidt, and M. Havrilla, "Geometrical optics polarimetric BRDF for dielectric and metallic surfaces," Opt. Exp., vol. 17, pp. 22138-22153 (2009).

[3] K. Torrance and E. Sparrow, "Theory for off-specular reflection from roughened surfaces," J. Opt. Soc. Am., vol. 57, pp. 1105-1114 (1967).

[4] J. Blinn, “Models of light reflection for computer sythesized pictures,” in Proc. SIGGRAPH, vol. 11, pp. 192-198 (1977).

[5] S. Pont and J. Koenderink, “Bidirectional reflectance distribution function of specular surfaces with hemispherical pits,” J. Opt. Soc. Am. A, vol. 19, pp. 2456-2466 (2002).

[6] S. Prasad, unpublished work (2013).

[7] Refractive Index Database <http://refractiveindex.info>. Retrieved on June 25, 2013.

[8] A. Barr, “Rigid Physically Based Superquadrics,” in *Graphic Gems III*, pp. 137-159, Academic Press (1992).

[9] A. Jakli, A. Leonardis, F. Solina, “Segmentation and Recovery of Superquadrics,” Kluwer Academic Publishers, (2000).

[10] T.-H. Tsai, private communication (2013).

[11] X.S. Yang, and D. Suash. “Cuckoo search via Lévy flights.” In Nature and Biologically Inspired Computing, 2009. World Congress on, pp. 210-214. IEEE, (2009).